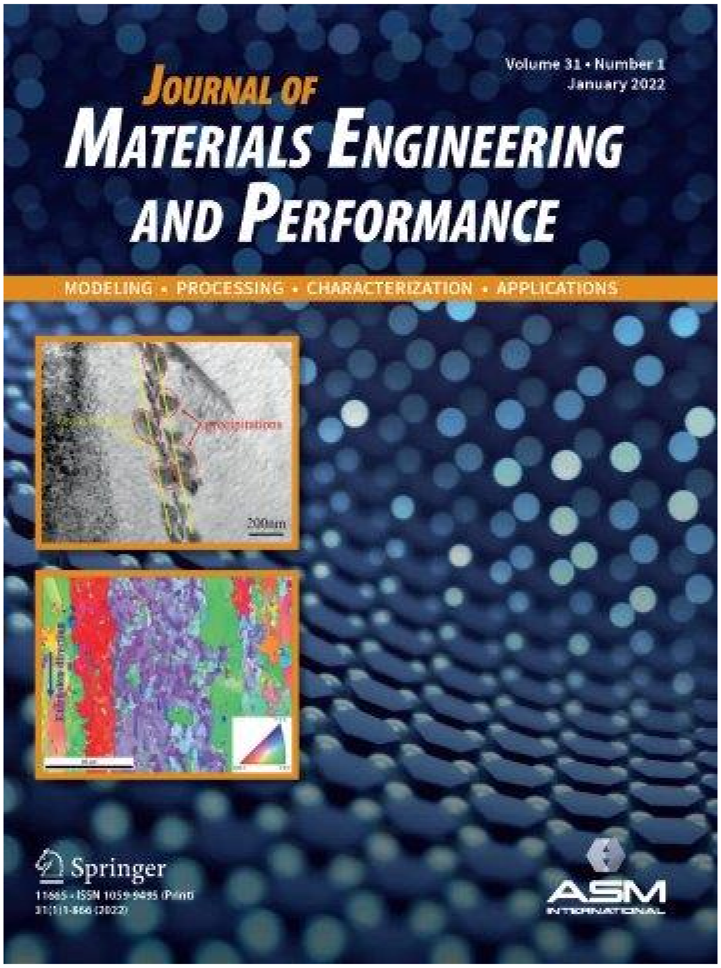

Tribocorrosion performance of Fe-based amorphous/CoCrFeNi-based high-entropy alloy composite coating by laser cladding

Journal:	*Journal of Materials Engineering and Performance*
Manuscript ID	JMEP-25-08-44041.R1
Manuscript Type:	Original Research Article
Date Submitted by the Author:	05-Oct-2025
Complete List of Authors:	Yang, Hanchi ; Tianjin University of Technology and Education tan, na; Tianjin University of Technology and Education Lu, Bingwen; Guangdong Academy of Sciences Institute of New Materials Li, Yang; Tianjin University of Technology and Education dong, xiaochuan; Tianjin University of Technology and Education Wang, Tao ; Tianjin University of Technology and Education Li, Guohe; Tianjin University of Technology and Education

Keywords:	Laser cladding, Fe-based amorphous alloy, High-entropy alloy, Tribocorrosion
Note: The following files were submitted by the author for peer review, but cannot be converted to PDF. You must view these files (e.g. movies) online.	
44041-Figures.zip	

Tribocorrosion Performance of Fe-Based Amorphous/CoCrFeNi-Based High-Entropy Alloy Composite Coating by Laser Cladding

Hanchi Yang[a,b], Na Tan[a*] , Bingwen Lu[c*], Yang Li[a,b], Xiaochuan Dong[b], Tao Wang[b], Guohe Li[b]

[a] Tianjin Key Laboratory of High Performance Precision Forming Technology and Equipment, Tianjin University of Technology and Education, Tianjin 300222, China

[b] National-Local Joint Engineering Laboratory of Intelligent Manufacturing Oriented Automobile Die & Mould, Tianjin University of Technology and Education, Tianjin 300222, China

[c] National Engineering Laboratory of Modern Materials Surface Engineering Technology, Guangdong Provincial Key Laboratory of Modern Surface Engineering Technology, Institute of New Materials, Guangdong Academy of Sciences, Guangzhou 510651, China

[*]Corresponding author: [a] Tianjin University of Technology and Education, Tianjin 300222, China

[c] Institute of New Materials, Guangdong Academy of Sciences, Guangzhou 510651, China

[a] E-mail address: tanna6786@163.com

[c] E-mail address: lubingwen@gdinm.com

Contact e-mail: tanna6786@163.com
Submitted: 21 August 2025 / Revised: 5 October 2025 / Accepted: 20 October 2025 /
Published online:
Materials Testing
JMEP-25-08-44041

Abstract:

In order to solve the problems of friction, corrosion and Tribocorrosion of equipment in extreme Marine environments, this study prepared $(FeSiBCr)_{1-x}$ $(CoCrFeNi)_x$ HEAs-amorphous composite coating on E690 Marine steel by laser cladding. The x= 25% coating achieved maximal amorphous content, finest crystalline grain size, and peak microhardness. Conventional sliding wear tests revealed its optimal tribological performance: lowest friction coefficient and 40% reduced wear rate versus pure iron-based amorphous coating, attributed to a transition from adhesive to abrasive wear mechanisms. In 3.5 wt.% NaCl, electrochemical tests confirmed superior corrosion resistance: noblest open-circuit potential and minimal corrosion current density. Subsequent tribocorrosion tests validated the superior performance of the x=25% coating, where the optimized dual-phase structure significantly inhibited detrimental microgalvanic corrosion and pitting initiation under simultaneous mechanical and chemical attack. This composition balances amorphous phase fraction and crystalline refinement, delivering synergistically optimized hardness, wear, corrosion, and tribocorrosion resistance for marine applications.

Keywords: Laser cladding, Fe-based amorphous alloy, High-entropy alloy, Tribocorrosion, corrosion

1. Introduction

With the development of marine resources and engineering technology, the durability and reliability of materials in extreme marine environments have become a research hotspot. Materials in fields such as deep-sea exploration, offshore oil platforms, wind turbines, and marine vessels often face severe friction and corrosion under complex environmental conditions, including prolonged seawater immersion, marine climate exposure, and wave impact.[1] These issues not only reduce material service life but also increase safety risks and economic losses. Therefore, improving the tribocorrosion resistance of materials under extreme marine environments is critical for enhancing the safety and longevity of marine engineering materials.

Amorphous alloys, also known as metallic glasses, are formed by rapid solidification of molten metal alloys. This process yields a glassy structure with short-range atomic disorder and long-range order. [2] Owing to their freedom from crystalline defects such as dislocations, stacking faults, and grain boundaries, amorphous alloys exhibit superior hardness and corrosion resistance compared to conventional crystalline alloys. [3] However, their glass-forming ability is critically dependent on alloy composition, elemental interactions, and manufacturing methods.[4]

Iron-based amorphous alloys demonstrate significant potential as novel engineering materials. They possess not only excellent mechanical properties but also outstanding surface characteristics and chemical stability, combined with relatively low production costs.[5] These comprehensive advantages have established them as a research focus in materials science. Nevertheless, existing studies indicate that the amorphous phase fraction in iron-based amorphous alloys is typically lower than in other amorphous systems. Enhancing this fraction is essential for improving their performance. [6]

High-entropy alloys (HEAs) amalgamate four or more dominant components in equiatomic or near-equiatomic proportions. Their fundamental distinction from conventional alloys lies in the multiprincipal-element effect, where high mixing entropy inhibits intermetallic compound formation and promotes solid-solution structures—typically FCC or BCC phases. [7-9] Among various HEA systems, CoCrFeNi HEAs exhibit widespread application potential owing to their favorable mechanical properties.

Existing research indicates that elevated cooling rates significantly enhance the synthesis of both CoCrFeNi HEAs and Fe-based amorphous alloys. [10] Employing a high-energy laser beam to melt and deposit metallic or non-metallic feedstock with precision onto substrates, laser cladding—an advanced surface modification method—yields high-performance coatings.[11] The process relies on rapid localized heating of the substrate surface while introducing cladding material via synchronous or preset powder feeding, achieving metallurgical bonding within the molten pool. Consequently, laser cladding features low dilution, high cooling rates, and a narrow heat-affected zone, which enables its suitability for preparing HEA and amorphous alloy coatings.[12-17] Based on current research [18-19], amorphous coatings can also be produced using methods such as thermal spraying and physical vapor deposition (PVD). However, these techniques present certain limitations. For instance, thermal spraying offers a relatively slow cooling rate, which results in poor amorphous forming ability and low amorphous content in the coating. Meanwhile, PVD suffers from a low deposition rate, restricting the coating thickness to the micron scale—much thinner than what can be achieved by laser cladding. Additionally, PVD equipment involves higher investment and maintenance costs. Therefore, this study considers laser cladding a more suitable method for preparing amorphous coatings.

Yuan et al. fabricated a CNT/FeCoNbBSi amorphous composite coating via laser cladding. With progressively elevated concentrations of the nickel-plated carbon nanotubes incorporated, the coating exhibited enhanced wear and corrosion resistance. [20] Wei et al. fabricated FeCrMoCBSi Fe-based amorphous composite coating on Q235 steel. The microhardness reaches $1313HV_{0.2}$. The frictional corrosion loss component is reduced by more than an order of magnitude compared to Q235, and the wear resistance is excellent. [21] Li et al. fabricated FeCrMoBSi amorphous coating on Q235 steel. Micro-Vickers hardness reaches $1400HV_{0.2}$ .Under the condition of reciprocating friction, the friction coefficient of the coating is stable at 0.45, the wear rate is 2.28×10^{-6} $mm^3/(N\cdot m)$, and the wear resistance is excellent. [22] The CoCrFeNi high-entropy alloy possesses considerable strength. However, its inadequate hardness prevents deployment in extreme environments. Previous studies have commonly introduced metallic or ceramic hard particles to increase hardness. Nevertheless, precise regulation of additive element proportions proves problematic, primarily owing to matrix element dilution during laser cladding. Fe-based amorphous alloy has good hardness. The fabricated coating, however, exhibits insufficient amorphous phase content. Unable to meet higher performance requirements . Consequently, this research fabricates HEAs/iron-based amorphous composite coatings via laser cladding. This work investigates the coating's microstructure, phase composition, microhardness, wear resistance, corrosion behavior, and tribocorrosion performance. These findings are anticipated to offer foundational insights for subsequent research on composite coatings.

2. Experimental process

2.1 Experimental preparation

Herein, E690 offshore steel was used as the matrix material. The size of E690 offshore steel is : 100mm×100mm×10mm. To secure the matrix material is not contaminated, sandpaper is used to polish and polish it carefully before the experiment. Ensure that there is no oxide layer on the substrate surface. In this study, the amorphous powder used to prepare the coating is FeSiBCr amorphous alloy powder. HEAs powder is CoCrFeNi HEAs powder. The proportion of composite powder is $(FeSiBCr)_{1-x}(CoCrFeNi)_x$. X is 0%, 25%, 50%, 75%. Table 1 presents the chemical compositions of distinct experimental materials employed in this study.

In this study, CoCrFeNi high entropy alloy powder and Fe-based amorphous powder were mixed and dried by planetary ball mill (XYQM-4L) and oven for 2 hours. The drying temperature is 120 ° C and the duration is 2 hours. Table 2 details the sample labeling methodology employed in this experiment. In this research, RC-LCD-4000 laser cladding system was used to prepare composite coatings. The optimum process parameters for preparing the composite coating were selected through the preliminary investigation of the process parameters. The specific parameters are: laser power 1500w, spot diameter 3mm, laser scanning rate 20mm/s, overlap rate 70%, powder feeding rate 16.8g/min. In this experiment, Argon served dual roles as the protective atmosphere and powder transport medium during cladding. The shielding gas flow rate is 10L / min, and the defocusing amount is 21 mm.

2.2 Test method

When the coating preparation is completed, each group of coatings are cut into the same size (10mm×10mm×10mm). After polishing the sample, aqua regia corrosion metallographic test was used. Field emission scanning electron microscopy (SEM, Zeiss Sigma 300) coupled with energy dispersive spectroscopy (EDS, Ultim Max) and metallographic microscopy characterized the composite coating's microstructure and elemental composition. Cu-Kα radiation was performed on the sample using a high-resolution X-ray diffractometer (Ultima IV). The scanning speed was 2 ° /min. Grazing-incidence XRD analysis characterized the composite coating's phase constitution across 10-100° incidence angles. Pseudo-Voigt fitting of Formula (1) quantifies the amorphous phase fraction within the coating.[23-24]

$$\mathrm{AP\%} = \frac{integral\ area\ of\ the\ background}{integral\ area\ of\ original\ diffraction} \qquad \text{Formula (1)}$$

The Vickers microhardness tester (Tukon2500) was used to test the microhardness of the composite coating with a load of 500 g and a loading time of 10 s. In order to reduce the experimental error, a hardness point is selected every 50 μm from the top to the bottom of the coating. Microhardness profiling characterizes the coating's hardness distribution along its depth profile, with the mean value subsequently calculated. Tribological properties were evaluated using a ball-on-disk tribometer (Lanzhou Huahui MS-M9000) under controlled conditions. The test method is axial reciprocating sliding of the coating surface by the grinding ball. The 6mm Si_3N_4 ball is selected as the grinding pair. The load is 10N, the single sliding distance is 5mm, the sliding frequency of the grinding ball is 2Hz, and the friction time is 30min. Post-tribological testing, 3D profilometer (Bruker Contour GT-K) scanning quantified the wear track cross-section on the coating surface. To minimize measurement deviations, repeat the scan three times and take the average. The wear rate of the coating can be calculated by Formula (2).

$$R_W = V_W/(S \times N) \qquad \text{Formula(2)}$$

Where V_w is the wear volume (m^3), S is the sliding distance (m), N is the load (N).

The electrochemical workstation (CS310M) employs a three-electrode system comprising a saturated calomel reference electrode, platinum plate auxiliary electrode, and sample working electrode, immersed in 3.5 wt.% NaCl electrolyte. At 30°C, the sample was soaked until the open circuit potential was stable, and the dynamic potential scanning rate was 0.5 mv/s.

Tribocorrosion testing of the coating was performed on a ball-on-disk tribometer(Lanzhou Huahui MS-M9000) integrated with an electrochemical workstation in corrosive media. The test method is axial reciprocating sliding of the coating surface by the grinding ball. The 6mm Si_3N_4 ball is selected as the grinding pair. The loading load is 10N, the single sliding distance is 5mm, the sliding frequency of the grinding ball is 2Hz, and the friction time is 30min. The electrochemical workstation employed a three-electrode configuration with a saturated calomel reference electrode, platinum sheet auxiliary electrode, and sample working electrode. The system was immersed in 3.5 wt.% NaCl electrolyte for corrosion testing. The experiment was carried out by potentiostatic method at 30°C. After the experiment, the characterization method of the corrosion friction morphology is the same as that of the conventional friction and wear experiment. In the titles of the charts in this article, the four groups of samples are respectively represented by S_A, S_B, S_C and S_D.

3. Results and discussion

3.1 Phase composition, microstructure and microhardness analysis

Fig. 1(a) depicts the XRD pattern of Fe-based amorphous alloy powder, revealing a fully amorphous structure. Fig. 1(b) compares the diffraction patterns of four composite coatings with distinct compositional ratios. The representation of each group of samples is shown in Table 1. The diffraction diagram reveals that the diffraction peaks near 45° across the four specimen sets show diffusion broadening, indicating that the coating is composed of amorphous phase and crystalline phase, which is consistent with the relevant reports. [25] Sample A is composed of α-Fe phase, Fe_2B and amorphous phase. Increasing the high-entropy alloy content induces progressive evolution toward a multiphase structure comprising α-Fe, FCC, and amorphous phases. When the composition ratio of high entropy alloy is 25%, it is evident that the peak intensities for α-Fe and Fe_2B are markedly attenuated while the corresponding peak at 45°undergoes broadening. This is because with the addition of high entropy alloy ratio, the confusion principle leads to the increase of amorphous phase.[26] And the high entropy alloy has the characteristics of inhibiting the production of metal compounds inside the structure.[27] When the proportion of high entropy alloy reaches 50%, the Fe_2B phase in the coating gradually disappears. B element does not react with Fe element and dissolves in FCC solid solution. At this time, the phase is composed of a small amount of α-Fe, amorphous phase and FCC phase. When the proportion of HEAs reaches 75%, the coating phase is transformed into only FCC phase and a minor amorphous phase constituent. This is because the proportion of iron-based amorphous alloy powder is too low, and the phase is dominated by CoCrFeNi high-entropy alloy.

The relative amorphous phase proportion in each group was quantified via Pseudo-Voigt fitting of XRD patterns, as presented in Fig. 1(c). [28] Existing research indicates that the high thermal input inherent to laser cladding constrains amorphous phase content in Fe-based amorphous alloy coatings, typically resulting in limited formation. [24] This demonstrates that with the increase of high entropy alloy, the amorphous content of the coating increased from 27.9 % to 46.3 % and then decreased to 42.7 %. The amorphous content of sample D with 75% high entropy alloy is only 21.4%, the content of which is inferior to that of pure Fe-based amorphous coating. The incorporation of CoCrFeNi increases the number of components in the system, thereby raising the mixing entropy of the alloy melt and reducing the crystallization driving force. As a result, the formation of an amorphous structure is facilitated under rapid cooling conditions. Additionally, the introduced components may alter the short-range ordered structure of the melt and enhance the resistance to both nucleation and growth of crystalline grains. However, when the HEA content becomes excessively high (x=75%), the inherent tendency of CoCrFeNi to form an FCC structure becomes dominant. Due to its own low glass-forming ability, this leads to a reduction in the overall amorphous phase content within the coating. Therefore, the volume fraction of the amorphous phase decreases as the proportion of the high-entropy alloy increases, and an excessively high HEA content adversely affects the formation of the amorphous phase in the coating.

Fig. 2 is the microstructure diagram for the four sample groups. Micrograph observation indicates that the superior and central zones of the four specimen coatings consist of equiaxed grains and dendritic structures. This is because the top of the coating is directly exposed to the environment when the molten pool is formed at the top of the coating, which can quickly dissipate heat, resulting in a rapid decrease in Thermal gradient (G), a higher solidification speed (R), and a lower G/R ratio. According to the solidification theory, it is easier to form dendrites or equiaxed grains under low G/R conditions. The solute in the upper region of the molten pool is enriched due to convection or evaporation, forming a significant component supercooling, which can also promote the growth of dendrite branches. The base of the coatings in the four sample groups is characterized by the presence of columnar crystals alongside a limited quantity of dendrites. This phenomenon can be attributed to the proximity of the base to the substrate, which serves as an effective conduit for heat dissipation, thereby sustaining a significant Thermal gradient (G). Concurrently, the solidification speed (R) remains low, resulting in a high G/R ratio that satisfies the conditions necessary for the growth of columnar crystals. The crystal structure of the substrate is used as a template to induce the epitaxial growth of the grains at the bottom of the molten pool along the heat flow direction (generally perpendicular to the substrate) to form columnar crystals. The solute diffusion in the bottom region is limited by the substrate, and the undercooled region of the composition is narrow, which inhibits the nucleation of equiaxed crystals, and the columnar crystals can continue to grow. A small amount of dendrites at the bottom may be formed due to local composition fluctuations or changes in heat dissipation direction. Among them, as shown in Fig. 2 (d), a gray area with discontinuous grain boundaries was found at the top of the coating of sample B. According to the existing research, it can be seen that the amorphous phase is a gray-white area with a large grain boundary interval, so it is speculated that it is an amorphous phase enrichment area. 30] This phenomenon can be ascribed to the rapid cooling rate at the coating surface, which promotes amorphous phase generation.. Sample B exhibits the highest amorphous content, and this amorphous phase is more distinctly evident in the scanning electron microscopy analysis.

As depicted in Fig. 3, the crystalline phase grain size of the four specimens initially decreases but subsequently increases with rising high-entropy alloy content. Average grain sizes are 5.39 μm (A), 2.23 μm (B), 2.29 μm (C), and 5.75 μm (D).With the addition of high entropy alloy, the grain size has been refined to a certain extent. The core mechanism is that a strong component undercooling is introduced and additional heterogeneous nucleation sites are provided, which increases the resistance of grain growth.The absence of these refinement mechanisms has resulted in sample A exhibiting the largest grain size, while the refinement effect observed in sample D is diminished due to the excessive incorporation of high entropy alloy powder.

As shown in Fig. 4(a), the hardness distribution of sample ABD is relatively uniform along its depth, whereas that of sample C exhibits significant fluctuations and an overall declining trend. This variability in sample C can be attributed to the non-uniform distribution of the amorphous phase, which is concentrated mainly in the upper and middle regions of the coating—areas known to possess higher hardness. Under the rapid cooling conditions of laser cladding, compositional segregation may occur, resulting in an inhomogeneous element distribution and the formation of hard metallic compounds preferentially in the top region. Meanwhile, closer to the substrate, heat dissipation from the molten pool slows, making it more difficult to form the amorphous phase. These factors collectively contribute to the pronounced fluctuations in hardness observed in sample C. In the schematics of Fig.4 (b), the average microhardness of the four groups of samples was 379.65HV (sample A), 833.86HV (sample B), 659.45HV (sample C) and 296.38HV (sample D), respectively. As evidenced in the micrograph, the composite coating's microhardness manifests substantial variation with escalating high-entropy alloy content, displaying an initial ascent succeeded by descent. Sample B exhibits peak microhardness, conversely sample D demonstrates minimal values. The change trend of microhardness is consistent with the change trend of amorphous phase content. This shows that the presence of amorphous phase can help to improve the microhardness of the coating. Furthermore, combined with the XRD pattern, sample A is composed of a certain amount of amorphous phase, α-Fe phase and metal compounds. Because the iron boron compound is a hard phase and has a certain degree of grain refinement, the hardness of sample A is higher than that of sample D without iron boron compound. However, with the addition of high-entropy alloy, the internal structure of the coating becomes chaotic, and a large number of amorphous phases are generated to improve the microhardness of the coating. Therefore, the microhardness of sample C is higher than that of sample A even if there is no iron boron compound. With the increase of the ratio of high entropy alloy, the α-Fe phase in the coating gradually decreases and the FCC phase gradually increases. Metals with a face-centered cubic crystal structure exhibit limited resistance to dislocation movement, possess a high capacity for plastic deformation, and can absorb significant amounts of energy prior to fracture. Consequently, materials with an FCC structure demonstrate remarkable ductility and toughness; however, they tend to have lower hardness compared to other crystalline structures.

3.2 Wear resistance

Fig. 5 (a) is the curve of friction coefficient of high entropy amorphous composite coating changing with time. The average friction coefficients of the four coatings are 0.69,0.65,0.67 and 0.72, respectively. Notably, the coating containing 25% high-entropy alloy (sample B) exhibits the lowest coefficient of friction, conversely the composite with 75% high-entropy alloy (sample D) demonstrates the highest tribological parameter. Minimal variation in frictional coefficients is observed across the four coatings. As the friction coefficient cannot be directly correlated to coating wear resistance, we analyzed the wear rates of all specimen groups. As indicated in Figure 5b, integrated with the preceding diagram, the coating's wear rate is minimal at 25% high-entropy alloy content, whereas it peaks at 75% HEA content. Conventionally, wear rate inversely correlates with microhardness. On the one hand, due to the high amorphous content of sample B, the microhardness of the coating is higher, so the wear rate is low and the coating is more wear-resistant. Comparison of Figures 3 and 4 indicates an inverse relationship between the overall wear rate trend and microhardness. Existing studies indicate that coexisting amorphous and crystalline phases in amorphous alloys enhance material hardness and toughness, consequently improving coating wear resistance. Additionally, metallic compounds within the coating contribute to wear performance. Thus, optimizing the balance among amorphous phase, crystalline phase, and metallic compound contents enhances the coating's wear resistance. Fig. 5 (d, e, f, g) are four groups of coatings. The three-dimensional morphology of the wear scar is observed by the white light interferometer. Fig. 5 (c) is a comparison of the wear cross sections of the four groups of coatings. It can also be seen from the three-dimensional topography that sample B exhibits optimal anti-wear performance.

Figure 6 is the conventional friction and wear morphology diagram. By observing Fig.6 (a, b, c, d), it is evident that the wear track of sample B is the narrowest in the four groups of samples, followed by sample C, and the wear track of sample D is the widest. The average widths of wear marks were 570.4,342.1,462.9 and 1332.1μm, respectively. Macroscopically, it can be judged that sample B has the best wear resistance and sample D has the least wear resistance. By observing Figs.6 (e, f, g, h), combined with Figs.7 and Table 3, it can be seen that there is a large adhesion zone on the surface of sample A and accompanied by an oxidation zone, so its wear form is mainly adhesive wear and oxidation wear. The wear scar surface of sample B and sample C is flat, and there are different degrees of furrows parallel to the sliding direction, indicating that the wear form of these two samples is abrasive wear. Sample D exhibits the most significant wear. Severe frictional force between the coating and the grinding ball results in localized thermal elevation. The oxide layer that forms as a result of the interaction between oxygen and the coating's surface serves a lubricating function. However, with the continuation of friction, this oxide layer is compromised. Subsequently, oxygen re-establishes contact with the coating's surface, leading to the formation of a new oxide layer, which exacerbates the extent of oxidative wear. Simultaneously, the fragmented oxide layer generates fresh abrasive particles, further intensifying the coating's abrasive wear; thus, the wear mechanisms encompass adhesive wear, abrasive wear, and oxidation wear.

In summary, incorporating an optimal amount of high-entropy alloy significantly enhances the wear resistance of iron-based amorphous alloys, with peak coating performance at 25% addition. Adhesive and tribo-oxidative mechanisms dominate the wear behavior of monolithic iron-based amorphous coatings. Composite coatings containing 25% and 50% high-entropy alloy powder exhibit abrasive wear. Conversely, the 75% high-entropy alloy composite coating demonstrates adhesive, abrasive, and oxidation wear mechanisms, exhibiting the lowest wear resistance.

3.3 Corrosion resistance

Fig.8 (a) shows the open circuit potential(OCP) and corrosion current density of the four groups of samples in 3.5wt% NaCl electrolyte solution. The OCP of sample A is the lowest, which is-0.347V, and the OCP of sample B is the highest, which is -0.161V. The corrosion current density of sample B is the lowest (3.788μA/cm²), whereas sample A demonstrates the highest magnitude at 6.24μA/cm².Figure 8 (b) shows the impedance values of the four groups of samples in 3.5wt% NaCl electrolyte solution. Generally, the diameter of the Nyquist diagram (Figure 8 (b)) corresponds to the corrosion resistance. The greater the diameter, the diminished corrosive reactivity, the higher the resistance, and the more challenging it is to transport the charge to the material's surface. It is found from the figure that the circle diameter of sample B is far exceeds that of the other three groups of samples, so sample B exhibits higher charge transfer resistance, indicating that it has Superior corrosion resistance. Fig.8 (c) presents the potentiodynamic scans for four specimen groups immersed in 3.5 wt% NaCl solution. The obtained data are calculated by Tafel extrapolation method. The corrosion current density of the test samples is shown in Fig.8 (a). The thermodynamic stability behavior of electrochemical corrosion is manifested by the open-circuit potential, a key parameter in corrosion potential measurements. Typically, an elevated open-circuit potential signifies enhanced chemical stability and a diminished corrosion tendency. Concurrently, a reduced corrosion current density correlates with a decreased corrosion rate, reflecting more effective corrosion resistance. The data presented in the preceding figure indicates that Sample B, which contains 25% high-entropy alloy, exhibits the most favorable corrosion resistance. This phenomenon can be ascribed to the intrinsic properties of the amorphous phase. The amorphous phase intrinsically lacks component segregation, secondary phase precipitation, and crystalline defects. Elevated amorphous content boosts the coating surface's thermal stability, thereby reducing corrosion susceptibility.

Further analysis of its corrosion mechanism showed that the OCP of sample A was the lowest (-0.347V), revealing that the passive layer stability was inadequate.Although the FeSiBCr amorphous alloy has a short-range ordered structure, the low Cr content is not enough to form a continuous and dense passivation film, and it is prone to local dissolution under Cl^- corrosion. The open circuit potential of sample B increased significantly to-0.161 V, which was due to the multi-principal synergistic effect of high-entropy alloy CoCrFeNi.When the content of Cr element was greater than 20at.%, the formation of Cr-rich oxide film was promoted. The addition of Co and Ni enhanced the repair ability and electron transport resistance of the passivation film, and the solid solution of Fe inhibited the local composition segregation, thus improving the thermodynamic stability. [31] The corrosion current density of sample B was the lowest (3.788 $\mu A/cm^2$), which was about 40 % reduction compared to sample A's value, evidencing significant suppression of the anodic corrosion rate. It is speculated that it can be attributed to the amorphous/high-entropy dual-phase composite structure of the coating. The amorphous phase provides a uniform passivation substrate, and the high-entropy phase forms the FCC phase/amorphous phase interface through multi-element co-diffusion, which hinders the penetration of Cl^- along the grain boundary. Concurrently, the addition of HEAs in the laser cladding process improves the fluidity of the molten pool, reduces porosity to a certain extent, enhances the coating's compactness, and obstructs corrosive medium permeation pathways. When the addition ratio of high-entropy alloy exceeds 25%, the degradation in corrosion resistance is speculated to be that the increase in the proportion of the cathode crystalline phase leads to the destruction of the continuity of the anode amorphous phase, forming a micro-galvanic corrosion pair, and the Cr depletion zone at the grain boundary of the high-entropy phase preferentially dissolves under the action of Cl^-.

In summary, an appropriate amount of high-entropy alloy can effectively enhance the corrosion resistance of iron-based amorphous coatings. Among them, the coating with 25% HEAs has the best corrosion resistance, which is attributed to the amorphous-high-entropy two-phase collaborative optimization mechanism. The coating's corrosion resistance diminishes as the high-entropy alloy proportion increases, yet consistently surpasses that of the iron-based amorphous coating.

3.4 Tribocorrosion resistance

Fig.9 (a) is the tribocorrosion coefficient curve of high entropy amorphous composite coating. All the friction coefficient curves fluctuate during the running-in period, and then become relatively stable during the stable wear period due to the formation of a friction film between the wear track and the friction pair. The ABCD friction coefficients of the samples were 0.54, 0.46, 0.65 and 0.61, respectively. Among them, the coating with a high-entropy alloy ratio of 25% (sample B) displays the minimal friction coefficient, and the composite coating containing 50% high-entropy alloy (sample C) exhibits the maximal friction coefficient. Due to the friction experiment in the corrosive solution, the solution acts as a lubricant to a certain extent during the experiment, resulting in a certain wear reduction effect, and the friction coefficient is also reduced to a certain extent compared with the conventional friction experiment. Among them, the friction coefficient of sample B decreased the most obviously and the lowest. Combined with the analysis of its wear form, this phenomenon is because the furrow caused by abrasive wear reduces the actual contact zone with its tribological counterpart, and the coating is immersed in the corrosion solution. The space gap generated by the furrow is soaked in the corrosion solution, which imparts moderate anti-wear properties. Therefore, the friction coefficient of sample B is lower and the change is larger than that of conventional friction. Due to the adhesive wear of sample A, the adhesive wear debris presents a agglomerated mud shape under the immersion of the corrosive solution, which also plays a certain anti-wear effect on the surface of the coating and reduces the friction coefficient. Results demonstrate enhanced tribological properties of the coating through optimal high-entropy alloy addition. As depicted in Fig. 9(b), the coating's wear rate initially declines before rising with increasing alloy content. Sample B containing 25% high entropy alloy exhibits minimal wear rates, denoting optimal tribological performance. Sample D containing 75% high entropy alloy demonstrates maximal wear rates, signifying inferior wear resistance. Combined with Fig. 9(c) wear cross-section morphology contrast and Fig. 9(d, e, f, g) three-dimensional morphology, analysis reveals that the wear volume of samples A, C, D is similar, while significantly differing from Sample B. This can be explained by the fact that sample B has the highest amorphous phase content and a certain amount of iron boron compounds, which makes it have high hardness and good wear resistance. Simultaneously, Sample B possesses the finest grain size, and such grain refinement effectively enhances the material's hardness and wear resistance.

Fig. 10 is the morphology of corrosion friction wear scar. Fig. 9(c) indicates that the wear widths of samples A, B, C, D were 462.9, 406.7, 556.7, 591.3 μm, respectively. Figure 11 (a) is the local amplification diagram in the dotted wire frame in Figure10 (e) and is tested by EDS. By observing Figure 9 (e, f, g, h) and combining Figure 3-11 with Table 4 analysis. Because the coating surface consists of numerous asperities, when two surfaces come into contact, only a limited number of these asperities actually engage. Under the direct application of load, the tips of the contacted asperities experience extremely high pressure and elevated temperatures, leading to plastic deformation of the material. This process can result in the destruction of the surface oxide film or contaminants, exposing fresh metal surfaces. The strong interaction between the atoms of the clean metal surfaces can lead to local welding between the asperities, particularly in the absence of lubrication or in cases of lubrication failure. Consequently, the wear mechanism observed in sample A is characterized by a combination of adhesive wear and oxidative wear. Different degrees of furrows were found on the wear marks of sample B and sample C. During the wear process, the normal load directly acts on the coating, and the accumulation of some dislocations leads to the formation of microcracks. Subsequently, the micro-cracks continue to propagate to form micro-brittle fracture and form wear debris. The wear debris accumulates on the wear scar and transforms into abrasive particles after accumulation. The micro protrusions of the grinding pair ploughed through the wear track, resulting in micro cutting and deep grooves on the wear track, confirming abrasive wear mechanisms for both specimens. At the same time, combined with Fig. 11 (c) and Table 4 EDS analysis, it can be seen that sample C also has slight oxidative wear. Fig. 11 (b) is the local amplification map in the dotted wire frame in Fig. 10 (h), and the EDS analysis shows that the wear of sample D is the most serious and there is oxygen enrichment. The hard abrasive particles scrape the surface to form a furrow, and the local high temperature and high pressure cause the adhesion transfer of the material, and the exposed fresh metal reacts with the oxygen in the environment to form an oxide layer. The wear form is the combination of adhesive wear, oxidation wear and abrasive wear. At the same time, no pitting corrosion was found in the first three groups of samples, indicating that although Cl^{-} corroded the coating under the action of 3.5 wt% NaCl solution, the overall corrosion resistance of the coating was excellent, and displayed no visible corrosion damage on the surface. There are honeycomb micropores in sample D, which proves that Cl^{-} causes pitting failure of the coating under the action of 3.5wt% NaCl solution.

The tribocorrosion mechanism of the composite coating was analyzed based on Fig.12. In sample A, the amorphous phase on the surface exhibits high hardness but limited toughness. During sliding against the Si_3N_4 ball, local shear band instability occurs, leading to material spalling and metal adhesion. Since the amorphous phase bears the primary contact stress, the load is distributed through elastic deformation. Meanwhile, the dispersed dendrites surrounding the amorphous regions function as "hard islands," locally resisting the ploughing action of the Si_3N_4 ball and reducing plastic flow. Dissolved oxygen in the saline environment, combined with frictional heating, promotes oxidation, resulting in oxidative wear on the coating. With prolonged immersion, a passivation film forms on the coating surface, providing resistance against Cl^{-} erosion. Wear debris generated from plastic deformation partially fills surface micro-pits, thereby delaying the penetration of corrosive media. As shown in Fig. 12(b), sample B possesses the highest proportion of amorphous regions, contributing to its high hardness and brittleness. Under repeated friction, angular wear debris forms, exacerbating abrasive wear as third-body particles. The limited presence of FCC phase enhances the coating's toughness, mitigating material loss from adhesion and oxidation. As friction continues, the surface passivation film undergoes repeated breakdown and reformation, establishing a positive feedback cycle of "corrosion–wear." The angular debris aggravates abrasive wear, which in turn accelerates the corrosion of freshly exposed metal. The superior corrosion resistance of the amorphous phase significantly weakens the accelerating effect of corrosion on wear, while the strengthening and toughening role of the FCC phase results in a smooth wear scar surface with shallow and narrow grooves. Due to the absence of grain boundaries and dislocations in the amorphous structure, Cl^{-} penetration along grain boundaries is hindered, explaining the lack of significant corrosion failure in the first three sample groups. Although sample A exhibits wear dominated by abrasion with minor oxidation, its overall performance is slightly inferior to that of sample B. This is attributed to structural weakening of the coating and reduced load-bearing and anti-ploughing capacity resulting from the increased crystalline phase content. As illustrated in Fig.12(d), the coating exhibits a mixed failure mechanism involving adhesion, oxidation, and abrasive wear, reflecting a complex degradation process. In this structure, the amorphous phase is distributed as isolated islands around crystalline regions. Coarse grains and low amorphous content lead to severe wear. With the coating dominated by the FCC phase, it exhibits low hardness and high toughness. The strong adhesive tendency causes material to be torn off by the counterface, resulting in significant volume loss and deep wear scars. The high density of grain boundaries accelerates oxidation in the saline environment. Detached metal particles and oxidized debris act as abrasives, further ploughing the coating surface. Additionally, honeycomb-like micropores observed on the surface of sample D indicate pitting corrosion, confirming mild pitting failure in this sample. The overlap of pitting pits and grooves suggests that corrosion exacerbates wear. This behavior is ascribed to the low amorphous content and coarse grain structure of sample D, which facilitate Cl^- ingress and promote material corrosion.

In summary, the inhibition of Cl^- penetration by changing the composition ratio to regulate the content of amorphous phase significantly enhances the coating's tribocorrosion performance. According to this study, the coating added with 25% high-entropy alloy has the best tribocorrosion resistance.

4. Conclusion

In this study, CoCrFeNi HEAs and Fe-based amorphous alloy composite coatings were prepared by laser cladding technology. The composite powder ratio is $(FeSiBCr)_{1-x}(CoCrFeNi)_x$, where X is 0 %, 25 %, 50 %, 75%. The microstructure, friction and wear properties, electrochemical corrosion properties and tribocorrosion properties of the composite coatings were characterized. The main results are as follows :

(1) The pure Fe-based amorphous coating with 0% HEAs powder and the composite coating with 25% HEAs powder are composed of α-Fe phase, Fe_2B compound and amorphous phase, and the diffraction peak of the latter at 45°is obviously broadened. The composite coating with 50% HEAs powder is composed of FCC phase, amorphous phase, a small amount of Fe_2B compound and α-Fe phase. The composite coating with 75% HEAs powder is composed of FCC phase and a small amount of amorphous phase. By SEM, the top and middle parts predominantly feature dendritic and equiaxed morphologies, and the bottom is composed of columnar crystals and a small amount of dendrites. The amorphous region is irregularly accompanied around the crystalline region.

(2) With the increase of the proportion of high entropy alloy powder, the microhardness increases first and then decreases. The composite coating with 25% high entropy alloy powder achieves peak microhardness and optimal wear resistance. This is attributed to the fact that the coating achieves maximal amorphous phase content, yielding superior hardness and tribological performance due to the characteristics of the amorphous phase without grain boundary dislocations.

(3) Electrochemical corrosion experiments show that the composite coating with 25% high-entropy alloy powder has the most excellent corrosion resistance, followed by the composite coating with 25% high-entropy alloy powder, and the iron-based amorphous coating without HEAs powder has the worst corrosion resistance. This is attributed to the amorphous-high entropy two-phase collaborative optimization mechanism. The high amorphous phase content can inhibit Cl- penetration, and an elevation in the high entropy alloy proportion leads to a reduction in the coating's corrosion resistance, but it is always better than that of the iron-based amorphous coating.

(4) The tribocorrosion properties experiment demonstrates that the composite coating with 25% high entropy alloy powder has the best tribocorrosion properties resistance, which is manifested in smaller wear rate, lower friction coefficient and no corrosion defects. It is found that there is a certain interaction between corrosion and friction. The corrosion defects produced by the coating with poor corrosion resistance accumulate in the wear marks to form a ' corrosion-wear ' positive feedback cycle. Hard oxides aggravate abrasive wear, while wear promotes fresh metal corrosion.

CRediT authorship contribution statement

Hanchi Yang: Methodology, Validation, Writing-original draft, Formal analysis, Writing-review & editing. Na Tan: Writing-original draft, Supervision, Writing-review. Bingwen Lu: Writing-original draft, Supervision, Writing-review. Yang Li: Resources. Xiaochuan Dong: Formal analysis. Tao Wang: Formal analysis. Guohe Li: Data curation.

Data availability

Data will be made available on request.

Declaration of Competing Interest

The authors declare that they have no known competing financial interests or personal relationships that could have appeared to influence the work reported in this paper.

Acknowledgements

The paper was financially supported by National Natural Science Foundation of China(52405211, 52375174), and Tianjin Science and Technology Plan Project(24JCQNJC00090, 22JCYBJC01620, 22JCYBJC01580,25JCQNJC00520).

5.Reference

1. A.A. Firoozi, D.O. Oyejobi, S. Avudaiappan, E.S. Flores, Enhanced durability and environmental sustainability in marine infrastructure: Innovations in anti-corrosive coating technologies, Results Eng. (2025): 105144.
2. F.C. Li, T. Liu, J.Y. Zhang, S. Shuang, Q. Wang, A.D. Wang, Y. Yang, Amorphous–nanocrystalline alloys: fabrication, properties, and applications, Mater. Today Adv.4 (2019): 100027.
3. C.A.C. Souza, D.V. Ribeiro, C.S. Kiminami, Corrosion resistance of Fe-Cr-based amorphous alloys: An overview, J. Non-Cryst. Solids.442 (2016): 56-66.
4. M. Pontoreau, O. Dezellus, S. Cardinal, J. Pelletier, R. Chiriac, F. Toche, P. Steyer, L. Gremillard, M. Vallée, X. Boulnat, Towards the additive manufacturing of Zr-based metallic glasses using liquid phase sintering: Reactivity and phase transformation kinetics at the crystalline/amorphous interface, J. Alloys Compd. 962 (2023): 171179.
5. J.Y. Liu, B.L. Li, S. Zhang, G.J. Liu, H. Ying, D. Li, C. Xie, X.Y. Zhang, X.L. Li, L. Wang, S.H. Wang, Fabrication of iron-based amorphous reinforced CoCrNi medium-entropy alloys by selective laser melting: Enhancement of mechanical properties and improvement of corrosion resistance, Intermetallics. 164 (2024): 108103.
6. T.Y. Xie, Y.T. Li, F.Y. Kong, C.H. Cheng, H.P. Wang, Z.M. Liu, A.D. Wang, Outstanding corrosion resistance of an Fe-based crystalline-amorphous nano-composite alloy, J. Alloys

Compd.1010 (2025): 178298.

7. E.P. George, D. Raabe, R.O. Ritchie, High-entropy alloys, Nat. Rev. Mater. 4, no. 8 (2019): 515-534.
8. J. Chen, P. Niu, T. Wei, L. Hao, Y. Liu, X. Wang, Y. Peng, Fabrication and mechanical properties of AlCoNiCrFe high-entropy alloy particle reinforced Cu matrix composites, J. Alloys Compd. 649 (2015): 630-634.
9. Y. Yu, J. Wang, J. Li, H. Kou, W. Liu, Characterization of BCC phases in AlCoCrFeNiTix high entropy alloys, Mater. Lett. 138 (2015): 78-80.
10. M.N. Nezhad, M.R. Aboutalebi, S.H. Seyedein, M. Barekat, Multi-criteria optimization of processing parameters in laser cladding of Al0. 5CoCrFeNiNb0. 5-Si0. 1 high entropy alloy coating, J. Mater. Res. Technol. 35 (2025): 6519-6536.
11. Z.U. Arif, M.Y. Khalid, E. Rehman, S. Ullah, M. Atif, A. Tariq, A review on laser cladding of high-entropy alloys, their recent trends and potential applications, J. Manuf. Process. 68 (2021): 225-273.
12. F.Y. Luo, W.Q. Shi, Z.Y. Xiong, J. Huang, Microstructure and properties analysis of AlCoCrFeNi high-entropy alloy/iron-based amorphous composite coatings prepared by laser cladding, J. Non-Cryst. Solids. 624 (2024): 122732.
13. H. Wang, D.K. Chen, X.H. An, S.J. Sun, Y.Z. Tian, Z.F. Zhang, A.G. Wang, J.Q. Liu, Deformation-induced crystalline-to-amorphous phase transformation in a CrMnFeCoNi high-entropy alloy, Sci. Adv. 2021, 7(14): eabe3105.
14. F.Y. Shu, L. Wu, H.Y. Zhao, L. Zhou, J. Zhang, Microstructure and high-temperature wear mechanism of laser cladded CoCrBFeNiSi high-entropy alloy amorphous coating, Mater. Lett, 2018, 211: 235-238.
15. X. Liang, X.L. Zhu, X. Li, R.D. Mo, Y.J. Liu, K. Wu, J. Ma, High-entropy alloy and amorphous alloy composites fabricated by ultrasonic vibrations, Sci China-Phys. Mech Astron, 2020, 63(11): 116111.
16. Z. Tan, L. Wang, Y. Xue, P. Zhang, T. Cao, X. Cheng, High-entropy alloy particle reinforced Al-based amorphous alloy composite with ultrahigh strength prepared by spark plasma sintering, Mater. Des, 2016, 109: 219-226.
17. P. Hruška, F. Lukáč, S. Cichoň, M. Vondráček, Oxidation of amorphous HfNbTaTiZr high entropy alloy thin films prepared by DC magnetron sputtering. J Alloys Compd, 2021, 869: 157978.
18. W.M. Guo, Y.P. Wu, J.F. Zhang, S.H. Hong, G.Y. Li, G.B. Ying, J. Guo, Fabrication and characterization of thermal-sprayed Fe-based amorphous/nanocrystalline composite coatings: an overview, J. Therm. Spray. Technol. 23(7), 1157-1180.
19. A. Roy, S. Wang, K. Komvopoulos, A review of plasma-assisted deposition methods for amorphous carbon thin and ultrathin films with a focus on the cathodic vacuum arc technique, J. Master. Res. 38(3), 586-616.
20. W.Y. Yuan, R.F. Li, Y.Y. Zhu, Y. Zhao, X.Q. Zhang, B. Liu, B.S. Zhang, Structure and properties of nickel-plated CNTs/Fe-based amorphous composite coatings fabricated by high-speed laser cladding, Surf. Coat. Technol. 438 (2022): 128363.

21. X.Q. Wei, S.X. Zheng, Y.D. An, S.L. Yu, G. Liu, J.B. Pu, Microstructure and tribocorrosion properties of Fe-based amorphous composite coatings fabricated by laser cladding, J. Mater. Sci. 59, no.9 (2024): 4039-4058.
22. K.Y. Li, J. Liang, J.S. Zhou, Preparation and characterization of laser cladded FeCrMoBSi amorphous composite coatings, Surf. Coat. Technol. 423 (2021): 127520.
23. H.N. Wang, Y.H. Cheng, R.W. Geng, B. Wang, Y.X. Chen, X.B. Liang, Comparative study on microstructure and properties of Fe-based amorphous coatings prepared by conventional and high-speed laser cladding. J. Alloys Compd, 2023, 952: 169842.
24. F. Chen, Z. Cai, G. Liu, X. Pang, L. Gu, J. Pu, Microstructure and tribological properties of FeCrBSi amorphous alloy coatings by ultra-high-speed laser cladding, J. Mater. Eng. Perform. (2024): 1-10.
25. M. Salaheldeen, A. Garcia-Gomez, M. Ipatov, P. Corte-Leon, V. Zhukova, J. M. Blanco, A. Zhukov, Fabrication and magneto-structural properties of Co2-based heusler alloy glass-coated microwires with high curie temperature, Chemosensors. 10, no. 6 (2022): 225.
26. S.Y. Chang, C.E. Li, Y.C. Huang, H.F. Hsu, J.W. Yeh, S.J. Lin, Structural and thermodynamic factors of suppressed interdiffusion kinetics in multi-component high-entropy materials, Sci.Rep.4, no. 1 (2014): 4162.
27. N. Liu, C. Chen, I. Chang, P, Zhou, X. Wang, Compositional dependence of phase selection in CoCrCu0. 1FeMoNi-based high-entropy alloys, Materials,.11.8(2018) :1290.
28. B. Manne, S. Bonrha, M.R. Ramesh, M. Kroshna, V.S. Balla, Solid state amorphization of Mg-Zn-Ca system via mechanical alloying and characterization, Adv. Powder Technol. 28.1 (2017): 223-229
29. F.Y Shu, L. Wu, H.Y. Zhao, S.H. Sui, L. Zhou, J, Zhang, W.X. He, P. He, B.S. Xu, Microstructure and high-temperature wear mechanism of laser cladded CoCrBFeNiSi high-entropy alloy amorphous coating, Mater. Lett. 211 (2018): 235-238.
30. F.H. Chen, Z. Cai, G. Liu, X. Pang, L. Gu, J. Pu, Microstructure and tribological properties of FeCrBSi amorphous alloy coatings by ultra-high-speed laser cladding, J. Mater. Eng perform. (2024): 1-10.
31. M. Peters, V.C. de Faria, L. Djumas, M. Brameld, E.G. Brodie, S. Thomas, C. Hutchinson, The development of Ni-Cr-W corrosion resistant alloys immune to sensitization, Corros. Sci. (2025): 113015.

Table1

Elemental composition of iron-based amorphous powder (at%)

Ele	Fe	Si	B	Cr
at%	Balance	11.75	5.45	2.37

Elemental composition of HEAs powder (at%)

Ele	Co	Cr	Fe	Ni
at%	25	25	25	25

Table2

Mark	Powder composition	
A	100%FeSiBCr	0%CoCrFeNi
B	75%FeSiBCr	25%CoCrFeNi
C	50%FeSiBCr	50%CoCrFeNi
D	25%FeSiBCr	75%CoCrFeNi

Table3

Ele	Fe	O	Cr	Si	Ni	Co
Sample A	70.9	18.3	8.3	2.5	/	/
Sample B	81.3	1.1	5.7	3.4	4.1	4.4
Sample C	84	3.5	2.0	5.1	5.1	0.4
Sample D	57.6	17.3	10.8	1.2	6.3	6.9

Table 4

	Fe	O	Cr	Si	Ni	Co
Sample A	62.9	26.0	7.2	3.9	/	/
Sample B	81.8	0.5	5.8	3.3	4.0	4.6
Sample C	78.5	10.1	2.0	3.9	2.0	3.2
Sample D	58.8	14.5	12.9	1.2	5.9	6.7

Fig. 1 X-ray diffraction pattern (a) XRD of iron-based amorphous powder (b) XRD of composite coating (c) Amorphous content of composite coating

Fig. 2 SEM micro-morphology of coating S_A (a) microstructure at the top (b) middle (c) bottom S_B (d) microstructure at the top (e) middle (f) bottom S_C (g) microstructure at the top (h) middle (i) bottom S_D (j) microstructure at the top (k) middle (l) bottom

Fig. 3 Grain size statistics of composite coating (a) S_A grain size statistics (b) S_B grain size statistics (c) S_C grain size statistics (d) S_D grain size statistics

Fig. 4 Microhardness diagram of composite coating (a) Microhardness diagram of each point of the four groups of coatings (b) Average microhardness statistics of the four groups of coatings

Fig. 5 Conventional friction experiment results (a) Friction coefficient comparison diagram (b) Wear rate comparison diagram (c) Comparison of cross-section wear morphology (d) (e) (f) (g) 3D morphology of four groups of samples

Fig.6 Macroscopic and microscopic abrasion morphology. Wear scar morphology of S_A (a)S_B (b) S_C(c) S_D(d) Local magnification of wear scar morphology of S_A(e) S_B(f) S_C(g) S_D(h)

Fig.7 EDS results of abrasion morphology (a) S_A (b) S_B (c) S_C (d) S_D Wear scar local amplification EDS results

Fig.8 Electrochemical corrosion test results (a) open circuit potential and corrosion density diagram (b) Nyquist diagram (c) potentiodynamic polarization curve diagram

Fig. 9 Corrosion friction experimental results (a) Friction coefficient comparison diagram (b) Wear rate comparison diagram (c) Comparison of cross-section wear morphology (d, e, f, g) Three-dimensional morphology of four groups of samples

Fig.10 Macroscopic and microscopic abrasion morphology. Wear scar morphology of SA (a) SB (b) SC(c) SD(d) Local magnification of wear scar morphology of SA(e) SB(f) SC(g) SD(h)

Fig.11 EDS results of abrasion morphology (a) S_A (b) S_B (c) S_C (d) S_D Wear scar local amplification EDS results

Fig.12 Tribocorrosion mechanism model. Tribocorrosion mechanism diagram of S_A (a) S_B (b) S_C (c) S_D(d)